THE JOURNAL OF BIOLOGICAL CHEMISTRY VOL. 291, NO. 25, pp. 13349–13359, June 17, 2016

Crystal Structure and Catalytic Mechanism of 7-Hydroxymethyl Chlorophyll *a* Reductase*

Received for publication, February 5, 2016, and in revised form, April 5, 2016 Published, JBC Papers in Press, April 12, 2016, DOI 10.1074/jbc.M116.720342

Xiao Wang[‡§] **and Lin Liu**[‡1]

From the [‡]*Key Laboratory of Photobiology, CAS Center for Excellence in Molecular Plant Sciences, Institute of Botany, Chinese Academy of Sciences, Beijing 100093 and the* [§]*University of Chinese Academy of Sciences, Beijing 100049, China*

7-Hydroxymethyl chlorophyll *a* reductase (HCAR) catalyzes the second half-reaction in chlorophyll *b* to chlorophyll *a* conversion. HCAR is required for the degradation of light-harvesting complexes and is necessary for efficient photosynthesis by balancing the chlorophyll *a*/*b* ratio. Reduction of the hydroxymethyl group uses redox cofactors [4Fe-4S] cluster and FAD to transfer electrons and is difficult because of the strong carbon-oxygen bond. Here, we report the crystal structure of *Arabidopsis* HCAR at 2.7-Å resolution and reveal that two [4Fe-4S] clusters and one FAD within a very short distance form a consecutive electron pathway to the substrate pocket. *In vitro* kinetic analysis confirms the ferredoxin-dependent electron transport chain, thus supporting a proton-activated electron transfer mechanism. HCAR resembles a partial reconstruction of an archaeal F_{420}-reducing [NiFe] hydrogenase, which suggests a common mode of efficient proton-coupled electron transfer through conserved cofactor arrangements. Furthermore, the trimeric form of HCAR provides a biological clue of its interaction with light-harvesting complex II.

The balance of chlorophyll metabolism is vital for plants to ensure an efficient photosynthesis and to support various biological processes (1). To this end, chlorophyll biosynthesis and degradation need to cooperate with the chlorophyll cycle, a process of interconversion between chlorophyll *a* and chlorophyll *b* (2–5). The chlorophyll *a*/*b* ratio is important for stabilization of the light-harvesting complexes (LHCs).[2] In general, an increase of the chlorophyll *b* level correlates with accumulation of LHCs and thus improvement of light usage efficiency in normal condition; excessive chlorophyll *b*, however, could impair the energy transfer pathway by replacing chlorophyll *a* in LHCs (6). In the chlorophyll cycle, both the forward (from chlorophyll *a* to chlorophyll *b*) and the backward conversions use 7-hydroxymethyl chlorophyll *a* (HMChl) as the intermediate (see Fig. 1*A*). Chlorophyll *a* oxygenase catalyzes two sequential oxidation reactions from the 7-methyl to the 7-formyl group (7, 8); chlorophyll *b* reductase and HMChl reductase (HCAR) catalyze the reverse two sequential reduction reactions (9, 10). In addition, the reverse reduction reactions are essential for LHC-II turnover because chlorophyll degradation precedes degradation of the LHC-II apoprotein, and the chlorophyll catabolic process starts from chlorophyll *a* (11–13). Direct interaction between HCAR and LHC-II has been observed in senescing chloroplasts (14).

HCAR is the last identified enzyme of the chlorophyll cycle (10). Bioinformatic studies have discovered that the HCAR homologues range from archaea to plants (15). They perform different roles, such as the F_{420}-binding subunit of F_{420}-reducing [NiFe] hydrogenase (Frh) in methanogenic archaea (16) and 3,8-divinyl (proto)chlorophyllide *a* 8-vinyl reductase (DVR) involved in (bacterio)chlorophyll biosynthesis (17, 18). The cofactors FAD and [4Fe-4S] cluster have been found to participate in electron transfer within Frh and DVR (18, 19). The structure of Frh from *Methanothermobacter marburgensis* has been solved by cryo-microscopy and crystallography (20–22). Frh is a heterotrimer, with subunit FrhA carrying a [NiFe] center, subunit FrhG carrying three [4Fe-4S] clusters, and subunit FrhB carrying one [4Fe-4S] cluster and one FAD. It has been suggested that the HCAR homologues adopt structures similar to that of FrhB, the F_{420}-binding subunit (19), but arrangements of the cofactors and hence the details of the electron pathway within HCAR remain unclear.

Here, the crystal structure of *Arabidopsis* HCAR reveals the ligating cysteines of the two [4Fe-4S] clusters, residues involved in FAD binding, and a deep substrate pocket adjacent to the flavin ring. We established a quantitative *in vitro* assay, confirmed the reduced ferredoxin (Fd_{red})-dependent reaction, and demonstrated that His^{417} and Asp^{237} are critical for the catalytic activity. This structural and biochemical characterization supports a proton-activated electron transfer mechanism. A structure-based phylogenetic analysis indicates that, in HCAR homologues, an efficient electron pathway and the usage of Fd_{red} as electron donor are kept despite the change of substrate specificity during evolution.

Experimental Procedures

Protein Expression and Purification—The gene of *Arabidopsis* HCAR (*At1g04620*) lacking sequence of the N-terminal 26 amino acid peptide was amplified by PCR. The product was inserted into pETMALc-H (23) with an introduced tobacco etch virus (TEV) cleavage sequence following the MBP-His_6 tag

* This work was supported by National Basic Research Program of China Grant 2011CBA00901, National Natural Science Foundation of China Grant 31370759, and Key Research Program Grant KGZD-EW-T05 from the Chinese Academy of Sciences. The authors declare that they have no conflicts of interest with the contents of this article.

[1] To whom correspondence should be addressed: Key Laboratory of Photobiology, CAS Center for Excellence in Molecular Plant Sciences, Institute of Botany, Chinese Academy of Sciences, 20 Nanxincun, Xiangshan, Beijing, 100093, China. Tel.: 86-10-62836483; E-mail: liulin@ibcas.ac.cn.

[2] The abbreviations used are: LHC, light-harvesting complex; HMChl, 7-hydroxymethyl chlorophyll *a*; HCAR, HMChl reductase; DVR, 3,8-divinyl (proto)chlorophyllide *a* 8-vinyl reductase; TEV, tobacco etch virus; SEC, size exclusion chromatography; FNR, ferredoxin-$NADP^+$-oxidoreductase; PCET, proton-coupled electron transfer.

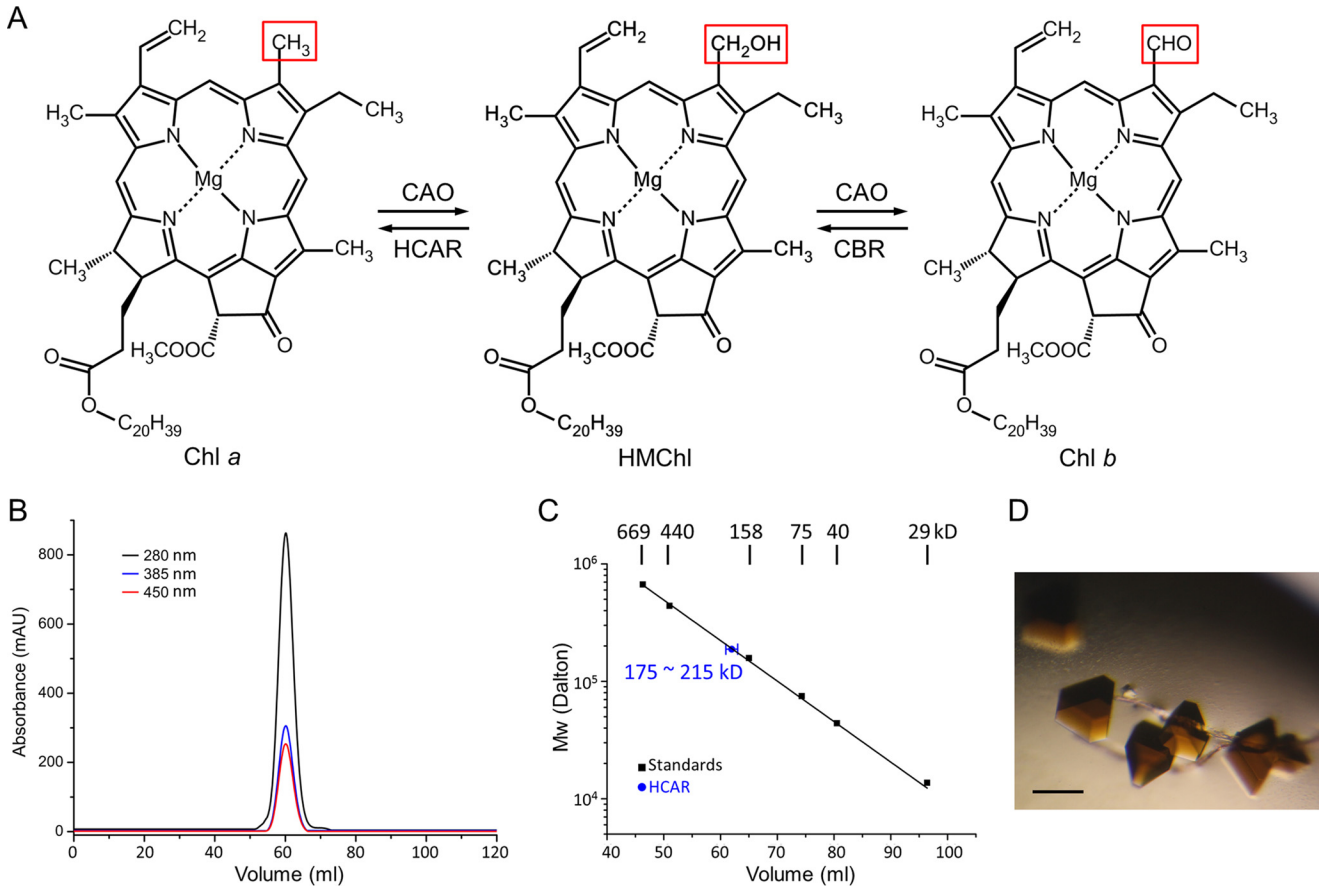

FIGURE 1. **Function, purification, and crystallization of HCAR.** *A*, interconversion of chlorophyll *a* and chlorophyll *b* with HMChl as intermediate. *CAO*, chlorophyll *a* oxygenase; *CBR*, chlorophyll *b* reductase. *B*, SEC profiles on a HiLoad 16/60 Superdex 200 column. The protein and its cofactors are monitored by absorbance at 280, 385, and 450 nm. *C*, calibration curve of logarithm of molecular mass as a function of elution volume. The HCAR elusion peak indicates an oligomeric state. *D*, the dark brown crystals of HCAR. The *scale bar* corresponds to 200 μm.

in the vector and then transformed into *Escherichia coli* BL21(DE3) cells. The expression of MBP-His_6-TEV-HCAR protein was induced with 0.2 mM isopropyl β-D-thiogalactopyranoside for ~16 h at 16 °C. Harvested cells were resuspended in buffer A (20 mM Tris-HCl, pH 7.0, and 500 mM NaCl) supplemented with 20 mM imidazole and disrupted by sonication. The cleared supernatant of cell lysate was incubated with buffer A-equilibrated nickel-nitrilotriacetic acid affinity column (Qiagen) for 1 h at 4 °C, and the recombinant proteins were eluted by 200 mM imidazole. The MBP-His_6 tag was cleaved by TEV protease. Protein aggregates and the MBP-His_6 tag were then removed by size exclusion chromatography (SEC; see below). The purity of HCAR protein was monitored by SDS-PAGE during purification. The purified protein was concentrated to 10 mg/ml and flash-frozen in liquid nitrogen for further crystallization or activity assay. The selenomethionine derivatives of HCAR were expressed at 25 °C supplemented with additional 10 mg/liter vitamin B_2 (Sigma-Aldrich) in the medium and purified as described above. The site-directed mutation of HCAR was generated with a Fast Mutagenesis System Kit (TransGen Biotech) using the MBP-His_6-TEV-HCAR plasmid as template. All mutated plasmids were sequenced to verify the desired mutations. The procedure for purification of the mutant proteins was the same as that of the wild type.

The fragment of *Arabidopsis* ferredoxin-$NADP^+$-oxidoreductase (FNR; *At1g20020*) lacking the N-terminal 55-amino acid peptide and the fragment of *Zea mays* ferredoxin (*FDX1*, GenBank™ code M73829) lacking the N-terminal 52-amino acid peptide were PCR-amplified. Both fragments were cloned into the pET-22b(+) (Novagen) expression vector, respectively. The expression procedure of FNR and ferredoxin were the same as that of HCAR, and both proteins were purified by a nickel-nitrilotriacetic acid column followed by SEC.

Size Exclusion Chromatography—A HiLoad 16/60 Superdex 200 column (GE Healthcare) was equilibrated with buffer A supplemented with 2 mM dithiothreitol. The protein elution profile was monitored by absorbance at 280 nm. The apparent molecular weight of HCAR was evaluated by comparison to globular protein standards (GE Healthcare) with known molecular weights. The protein standards are thyroglobulin, ferritin, aldolase, conalbumin, ovalbumin, and carbonic anhydrase. Comparison of the HCAR peaks from triplicate experiments with the calibration curve yielded an apparent molecular weight.

Chlorophyll Preparation—Chlorophylls were extracted with acetone from spinach leaves. Chlorophyll *b* was separated by a 200-mesh silica column with hexane/ethyl acetate (Sigma-Aldrich) in 2:1 (v/v) ratio as the elution agent. HMChl was prepared by reducing chlorophyll *b* with $NaBH_4$ (32). 1 mg of chlorophyll *b* was dissolved in 10 ml of methanol containing 0.5 mg of $NaBH_4$ and incubated for 2 min at room temperature. The reaction was stopped by adding 10 ml of saturated NaCl solu-

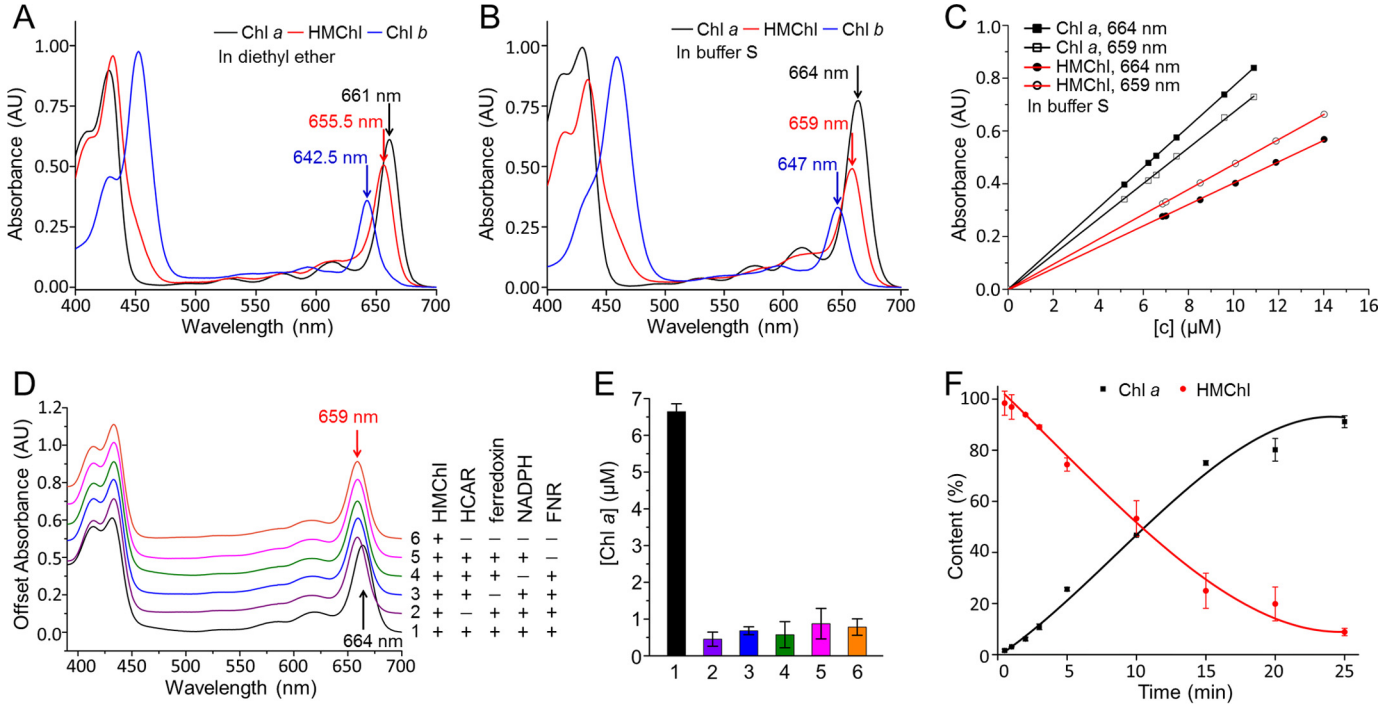

FIGURE 2. **Establishment of a quantitative activity assay for HCAR.** *A* and *B*, spectral comparison of purified chlorophylls in diethyl ether (*A*) and in buffer S (*B*). *C*, the calibration line of absorbance *versus* concentration of chlorophyll *a* and HMChl in buffer S. The same standard series of chlorophyll *a* or HMChl were measured at 664 and 659 nm. The extinction coefficient is derived from the slope by the least squares method. *D*, the absorption spectra of six *in vitro* HCAR activity experiments. The presence or absence of a component (50 μM HMChl, 15 μM HCAR, 10 μM ferredoxin, 1 mM NADPH, 10 μM FNR) is indicated by + or −, respectively. The reaction was stopped with four parts acetone, and then the liquid phase was spectroscopically monitored. *E*, product contents of the six experiments after the 15-min reaction. The experiment order is same as that in *D*, and the same color scheme is used. The contents of chlorophyll *a* are calculated from the absorbance value at 659 and 664 nm. The *error bars* represent the S.D. from three independent experiments. *F*, progress curve of the HCAR-catalyzed reaction. The reaction with approximate 3-fold excess of HMChl was prepared as in experiment 1 in *D*, and three replicates were conducted. The contents of HMChl and chlorophyll *a* are calculated from the absorbance value at 659 and 664 nm. *Chl*, chlorophyll.

tion, and the products were transferred into diethyl ether and dried by nitrogen. The crude products of chlorophyll *a*, chlorophyll *b*, and HMChl were purified by HPLC on a SunFire Prep C18 OBD column (5 μm, 19 × 250 mm; Waters) with methanol as the elution agent. Purified chlorophylls were pooled and dried by nitrogen. The steps of chlorophylls preparation need to avoid light.

Determination of Extinction Coefficients—To establish the activity assay, we first characterized the spectroscopic properties of chlorophyll *a*, chlorophyll *b*, and HMChl in buffer S (5 mM Tris-HCl, pH 7.5, 30 mM NaCl, 0.02% Triton X-100, and 80% acetone). The absorbance peaks of HMChl and chlorophyll *a* are at 655.5 and 661 nm in diethyl ether, and at 659 and 664 nm in buffer S. We then determined the extinction coefficients of HMChl and chlorophyll *a* at 659 and 664 nm in buffer S, respectively. The molar extinction coefficient (ϵ) of chlorophyll *a* at 664 nm in 80% aqueous acetone is 76.79 mM^{-1} cm^{-1} (33). The ϵ value of chlorophyll *a* at 664 nm in buffer S is 76.98 ± 0.70 mM^{-1} cm^{-1}. The ϵ value of HMChl at 655.5 nm in diethyl ether is 61.10 mM^{-1} cm^{-1} (34). The ϵ values of HMChl at 655.5 and 659 nm in buffer S are 44.57 ± 0.65 and 47.30 ± 0.39 mM^{-1} cm^{-1}. By calibrating with a series of chlorophyll *a*/HMChl standards at 664 and 659 nm in buffer S, the ϵ value of chlorophyll *a* at 659 nm in buffer S is 66.98 ± 0.68 mM^{-1} cm^{-1}, and the ϵ value of HMChl at 664 nm in buffer S is 40.24 ± 0.31 mM^{-1} cm^{-1}. Using an experimental scheme described by Porra *et al.*

TABLE 1

Data collection and refinement statistics

Highest resolution shell values are shown in parentheses.

	Native HCAR	SeMet-HCAR
Data collection		
Space group	$P3_2$	$P3_2$
Cell dimensions		
a, *b*, *c* (Å)	89.1, 89.1, 273.3	89.5, 89.5, 292.7
α, β, γ (°)	90, 90, 120	90, 90, 120
Wavelength	0.9793	0.9793
Resolution (Å)	50 − 2.70 (2.80 − 2.70)	50 − 3.20 (3.31 − 3.20)
R_{sym} or R_{merge} [a]	0.105 (0.571)	0.112 (0.812)
$I/\sigma I$	11.6 (2.3)	37 (4.8)
Completeness (%)	99.6 (99.9)	100 (100)
Redundancy	3.2 (3.2)	22.8 (23.4)
Refinement		
Resolution (Å)	44.6 − 2.70	
No. reflections	65245	
R_{work} [b]/R_{free} [c]	0.202/0.246	
No. atoms		
Protein	19280	
Ligand/ion	414	
Water	622	
B-factors		
Protein	17.4	
Ligand/ion	10.0	
Water	13.9	
Root mean square deviations		
Bond lengths (Å)	0.005	
Bond angles (°)	0.852	

[a] $R_{merge} = \Sigma_{hkl}\Sigma_i|I_i(hkl) - <I(hkl)>|/\Sigma_{hkl}\Sigma_i I_i(hkl)$, where $I_i(hkl)$ is the *i*th observation of reflection hkl and $<I(hkl)>$ is the weighted intensity for all observations *i* of reflection *hkl*.

[b] $R_{work} = \Sigma||F_o| - |F_c||/\Sigma|F_o|$, where F_o and F_c are the observed and calculated structure factors, respectively.

[c] R_{free} is the cross-validated *R* factor computed for a test set of 5% of the reflections, which were omitted during refinement.

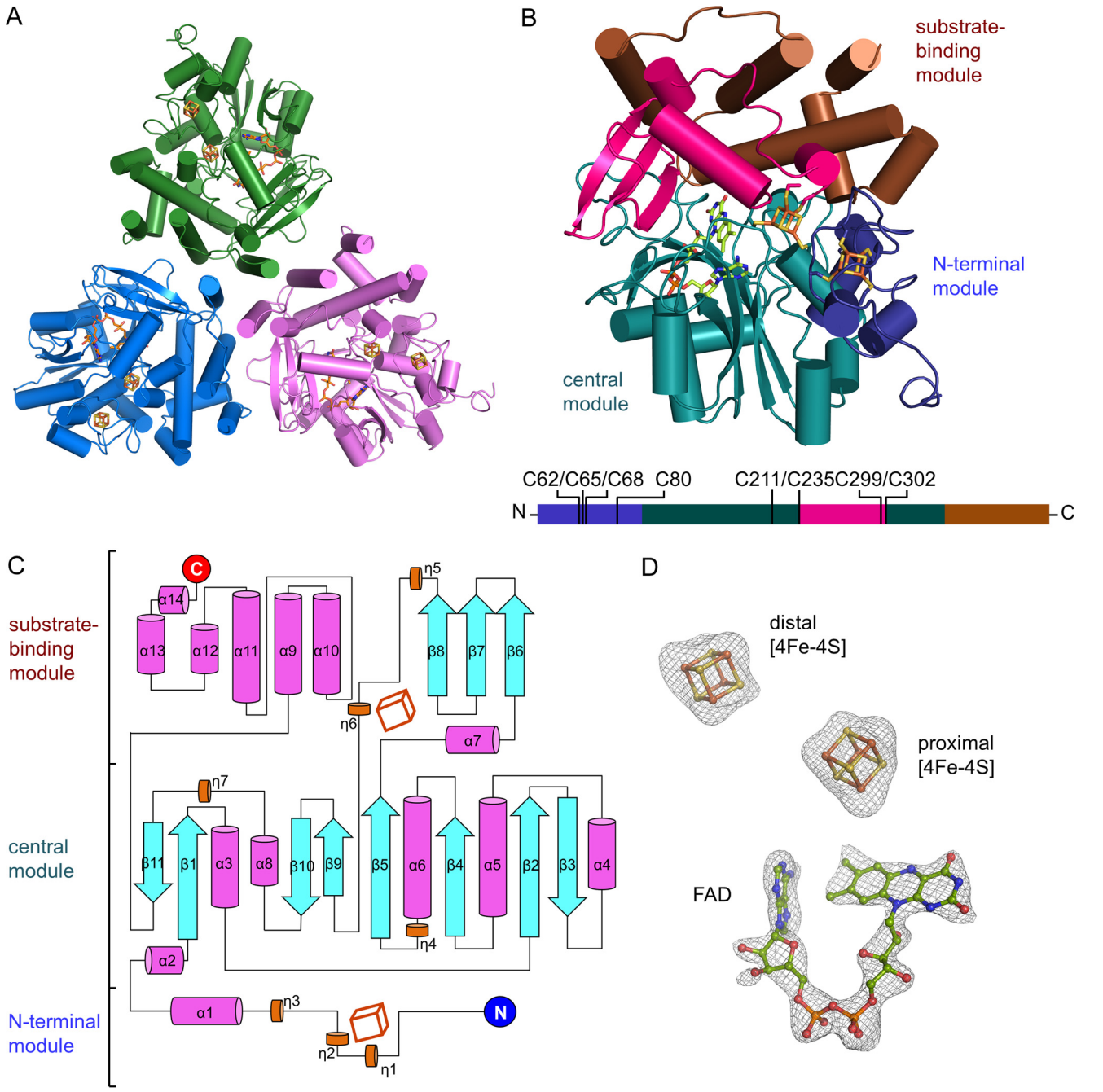

FIGURE 3. **Structure of HCAR.** *A*, HCAR trimer in trefoil shape. Protomers are colored in *green*, *blue*, and *purple*, respectively. *B*, structure of an HCAR protomer. Three functional modules are color-indicated. The [4Fe-4S] clusters with their ligating cysteines and the redox cofactor FAD are shown as sticks. An overview of the functional modules of HCAR is shown at the *bottom* with the ligating cysteines indicated. The overall structure is divided into three functional modules, which are the N-terminal module (residues 27–100), the central module (101–235, 303–358), and the substrate-binding module (236–302, 359–462). *C*, topology of the secondary structure elements of HCAR. The N and C termini are indicated as *blue* and *red circles*. α-Helix and 3_{10} helix are shown as *magenta* and *orange cylinders*, and β-strands are shown as *cyan arrows*. Two [4Fe-4S] clusters are shown as *cubes*. *D*, defined electron density of the cofactors. The $|F_o| - |F_c|$ omit map is contoured at 3σ as *gray mesh*.

(33), by measuring the absorbance at 659 and 664 nm ($A_{659\,nm}$ and $A_{664\,nm}$) of a chlorophyll *a*/HMChl mixture, the concentration of chlorophyll *a* and HMChl can be calculated by using the following equations.

$$[\text{HMChl}] = 81.35A_{659\,nm} - 70.79A_{664\,nm} \quad \text{(Eq. 1)}$$

$$[\text{chlorophyll } a] = 49.99A_{664\,nm} - 42.52A_{659\,nm} \quad \text{(Eq. 2)}$$

In Vitro Activity Assay—The HCAR activity assay was performed in 100 μl of buffer B (25 mM Tris-HCl, pH 7.5, 150 mM NaCl, and 0.1% Triton X-100), with 50 μM HMChl, 10 μM FNR, 10 μM ferredoxin, 1 mM NADPH, and 15 μM HCAR. The reaction mixture was incubated at 25 °C for 15 min before 400 μl of acetone was added, which yielded the mixture in buffer S (20% buffer B and 80% acetone). The chlorophylls were extracted into liquid phase by violent vortexing,

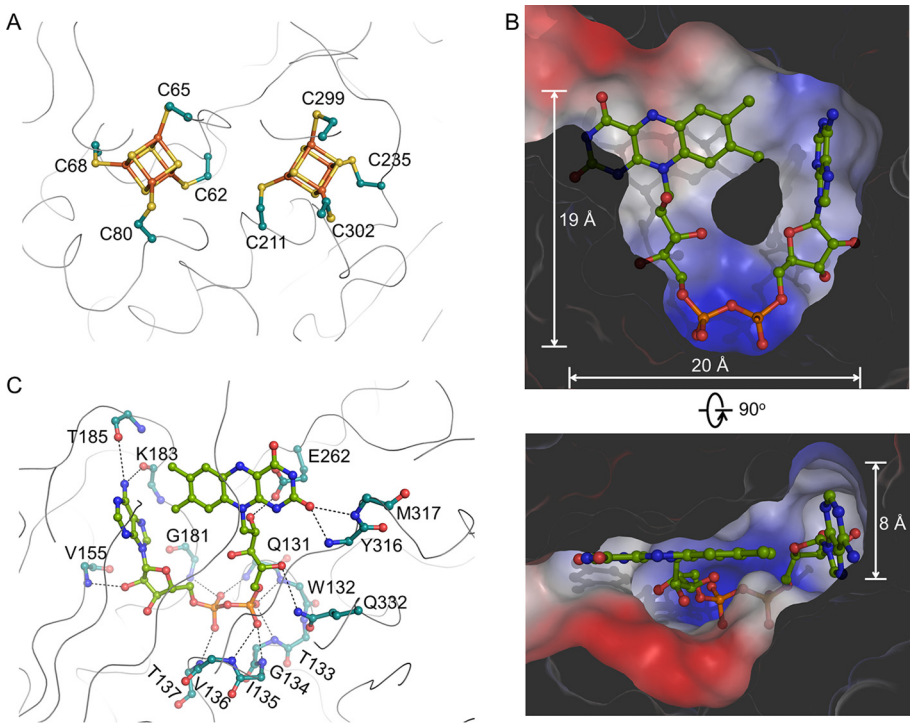

FIGURE 4. **Cofactor interactions.** *A*, details of the two [4Fe-4S] cluster-binding sites. *B*, the FAD-binding pocket. The surface of HCAR is colored according to the electrostatic potential. *C*, the environment of the FAD cofactor (*green sticks*). The side chain atoms of residues whose backbone atoms participate in FAD binding are not shown.

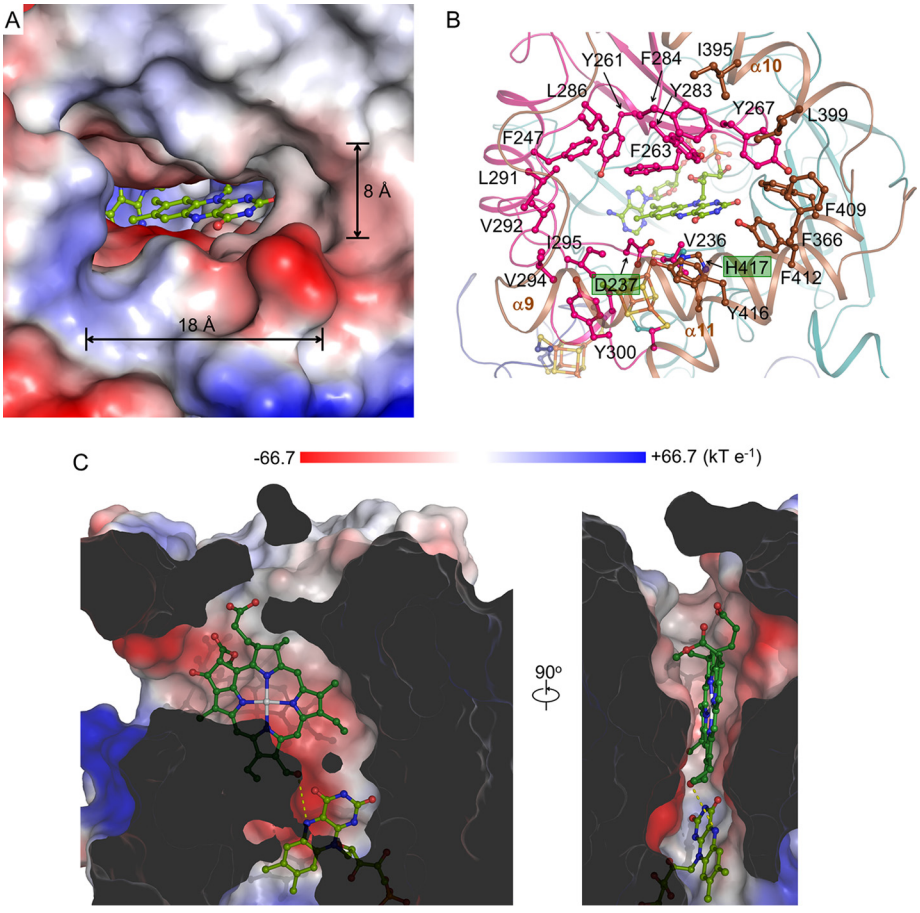

FIGURE 5. **The substrate pocket.** *A*, overall shape of the substrate pocket. *B*, side chains of the constituting residues and FAD are shown in stick. His^{417} and Asp^{237} are indicated. *C*, clipped surface representation of the substrate pocket. A docked HMChlide is shown in stick. The N_5 atom of FAD and the oxygen atom of the hydroxymethyl group are linked by a *yellow dashed line*. The surface of HCAR is colored according to the electrostatic potential.

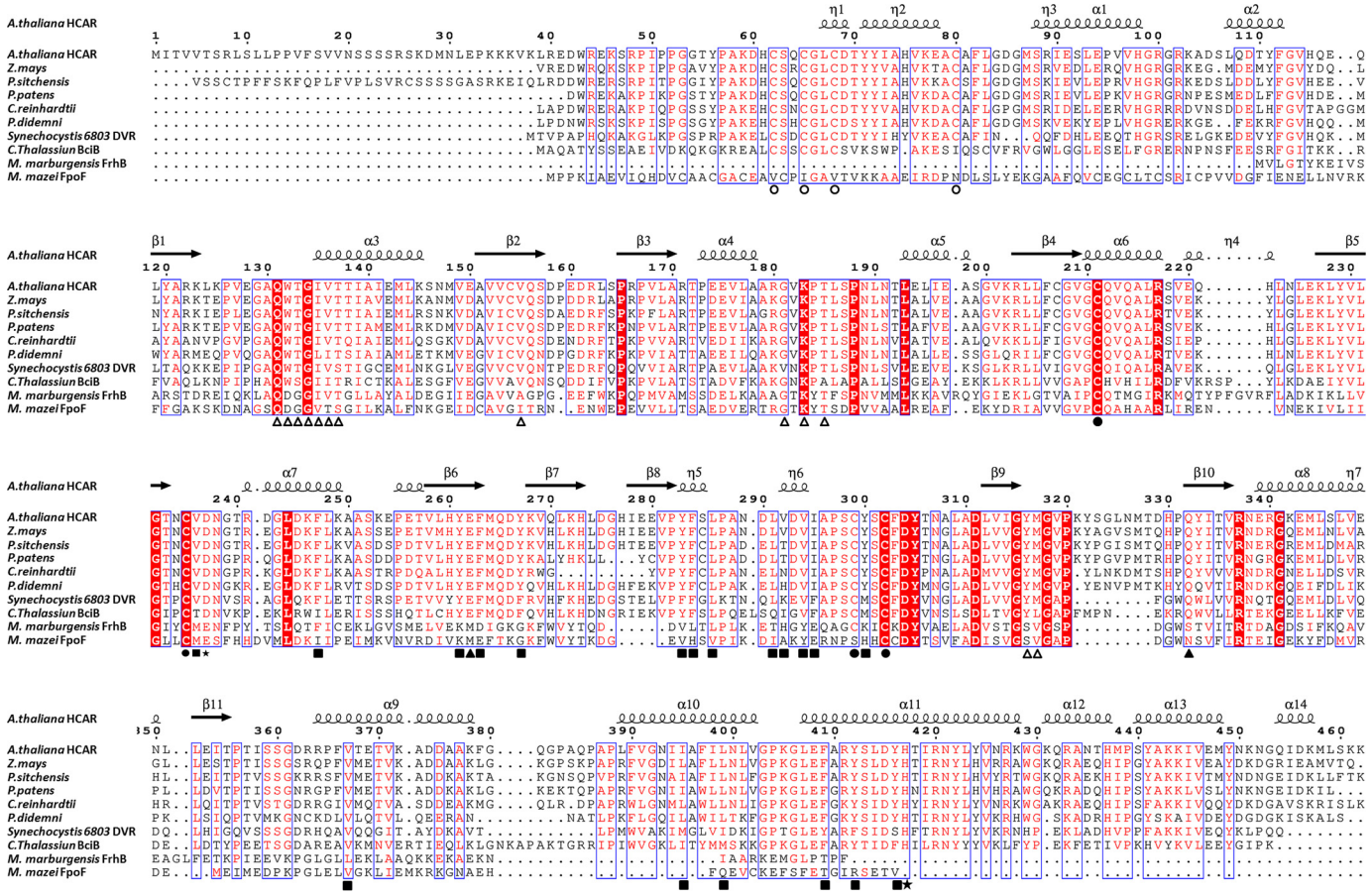

FIGURE 6. **Sequence alignment.** The amino acid sequences of HCAR homologues from 10 species are aligned. The ligating cysteines of the distal and proximal [4Fe-4S] clusters are labeled by *empty* and *solid circles*, respectively. The FAD-binding residues whose backbone atoms are involved in FAD interaction are indicated by *empty triangles*, and those whose side chain atoms are involved are indicated by *solid triangles*. Residues forming the substrate pocket are indicated by *solid squares*. His^{417} and Asp^{237} are labeled with *stars*.

whereas the proteins were denatured by acetone. After centrifugation at 16,000 × *g* for 10 min, the separated supernatant containing the chlorophylls was analyzed by full-wavelength scanning or monitored by the absorption at 664 and 659 nm in a 1-cm cuvette.

Crystallization, Data Collection, Structure Determination, and Refinement—Initial crystallization screening was performed by the vapor diffusion method in a sitting drop consisting 1 μl of HCAR protein (10 mg/ml) mixed with 1 μl of well solution at 289 K. Dark brown crystals appeared after 5 days under 0.2 M $MgCl_2$, 0.1 M Tris-HCl, pH 8.5, 25% (w/v) polyethylene glycol 3350, 3% (v/v) ethylene glycol, and its quality was improved by seeding method. Before being flash-frozen in liquid nitrogen, the crystals were transferred step by step into drops of the mother liquid supplemented with 5, 10, and 20% (v/v) glycerol. All x-ray diffraction data sets were collected at Beamline BL17U of Shanghai Synchrotron Radiation Facility at a wavelength of 0.9793 Å at 100 K. The data were integrated and scaled by HKL2000 (HKL Research, Inc.). 66 selenium atoms in six HCAR molecules per asymmetric unit were determined by AutoSol in PHENIX suite (24, 25). The identified selenium sites were then refined, and the initial model were generated by AutoBuild (26). The missing residues were built manually using Coot (27) according to the $2|F_o| - |F_c|$ and $|F_o| - |F_c|$ electron density maps. The structure was then refined using phenix.refine (28). The overall quality of the structure was assessed by MolProbity (29), and 95.86, 3.86, and 0.28% of the residues were in the most favored, additional allowed and disallowed regions of the Ramachandran plot, respectively. Structure determination and refinement statistics are listed in Table 1. The structure and diffraction data have been deposited in the Protein Data Bank (code 5DQR). The protein structure figures were prepared by PyMOL (Schrödinger).

Substrate Docking—In silico docking of a 7-hydroxymethyl chlorophyllide *a* (HMChlide, HMChl without the phytol tail) to HCAR was performed with the program AutoDock Vina 1.1.2 (30). The HMChlide coordinates were adapted from chlorophyll *b*. Protein coordinates were taken from chain B of the HCAR structure. Prior to simulation, hydrogen atoms, Gasteiger partial charges and ligand torsions, especially the torsion of the C–O bond that is different from the C=O bond in chlorophyll *b*, were added using the program AutoDockTool (31). During simulation, the protein structures were kept rigid, and grid maps were calculated using 18 × 16 × 22 grid points with spacing of 1.0 Å. Grids were minimized and centered such that they barely covered the substrate pocket, and the most plausible docking result was selected based on the steric accessibilities of the substrate and the calculated binding affinity energy.

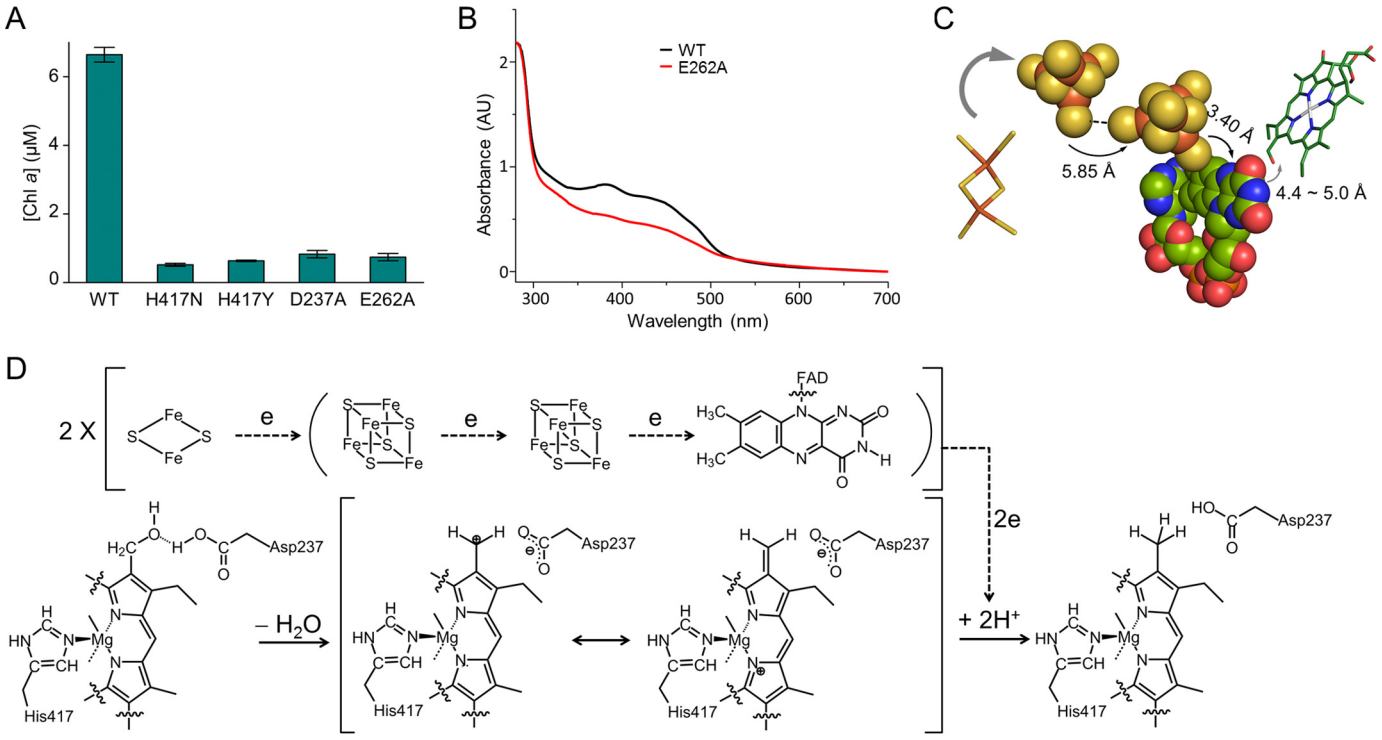

FIGURE 7. **Catalytic mechanism.** *A*, assays for the critical residues involved in HCAR catalysis. The data are presented as the means ± S.D. of three independent experiments. *B*, spectra of HCAR proteins. E262A mutant protein has decreased absorbance between 300 and 500 nm, consistent with the fact that it contains less cofactor than the wild type HCAR. *C*, electron transfer pathway. The [4Fe-4S] clusters and FAD are shown in *sphere model*. The [2Fe-2S] cluster of Fd and the substrate HMChlide are shown as *sticks*. The distances between each element are indicated. *D*, proposed catalytic mechanism of HCAR. *Dashed lines* show the electron flow path from [2Fe-2S] cluster of ferredoxin to substrate via two [4Fe-4S] clusters and FAD.

Sequence Analysis—Amino acid sequences were aligned using Clustal Omega (35). The secondary structure elements were recognized by DSSP program (36), and the figure was created by ESPript 3 (37).

Phylogenetic Analysis—For the phylogenetic analysis, the midpoint-rooted neighbor-joining tree was generated using MEGA 4 software (38), with the following parameters: bootstrap (500 replicates), complete deletion, Poisson model, and uniform rates. The accession numbers are: NP_171956.2 (*Arabidopsis thaliana* HCAR), XP_008681058.1 (*Z. mays*), ABR16627.1 (*Picea sitchensis*), XP_001770443.1 (*Physcomitrella patens*), XP_001699546.1 (*Chlamydomonas reinhardtii*), WP_040945152.1 (*Prochloron didemni*), WP_010873198.1 (*Synechocystis* PCC 6803 DVR), ACF13672.1 (*Chloroherpeton thalassium* BciB), WP_013296464.1 (*M. marburgensis* FrhB), and AAF65743.1 (*Methanosarcina mazei* FpoF).

Results

HCAR Is a Trimer—The purified mature *Arabidopsis* HCAR is of 49 kDa, and the apparent molecular mass according to SEC elution profile is 195 ± 20 kDa (Fig. 1, *B* and *C*), which suggests a trimeric or tetrameric state. Given the non-globular shape of an HCAR trimer (see below), the apparent molecular weight is consistent with a trimer state. The purified protein is colored dark brown, indicating the binding of cofactors [4Fe-4S] and FAD. The yielding HCAR crystals also exhibit dark brown color (Fig. 1*D*).

Establishment of an in Vitro Assay—To quantitatively characterize the activity of HCAR, we first established an assay on the basis of absorption spectra (Fig. 2, *A*–*C*). The assay was performed in an aqueous system at near neutral pH. The peak absorbances of substrate HMChl and product chlorophyll *a* are at 659 and 664 nm in our spectrum measurement buffer. The corresponding molar extinction coefficients are 47.30 ± 0.39 $mM^{-1}\ cm^{-1}$ at 659 nm and 40.24 ± 0.31 $mM^{-1}\ cm^{-1}$ at 664 nm for HMChl and are 66.98 ± 0.68 $mM^{-1}\ cm^{-1}$ at 659 nm and 76.98 ± 0.70 $mM^{-1}\ cm^{-1}$ at 664 nm for chlorophyll *a*.

In this *in vitro* assay system, Fd_{red} was obtained by supplying NADPH and FNR. All the components of the assay, including ferredoxin, FNR, NADPH, and HCAR, are indispensable for the conversion of HMChl to chlorophyll *a*, as demonstrated by the shift of maximum absorption from 659 to 664 nm (Fig. 2*D*). The contents of the product chlorophyll *a* can be calculated (Fig. 2*E*). The reaction shows a typical first order catalytic profile when excess HMChl is supplied (Fig. 2*F*).

Overall Structure of HCAR—The molecular replacement method using coordinates of the 31-kDa FrhB as template did not find a solution. The structure was determined using single-wavelength anomalous diffraction method (39) and refined to 2.7 Å (Table 1). An HCAR trimer is in a trefoil shape (Fig. 3*A*). Each protomer shows a compact fold with fourteen α-helices, seven 3_{10}-helices, and eleven β-strands (Fig. 3, *B* and *C*). This compact structure can be further divided into three functionally discrete modules: an N-terminal module holding a [4Fe-4S] cluster, a central module engulfing the FAD cofactor, and a substrate-binding module composed of a C-terminal helical bundle and an insertion region from the central module. At the

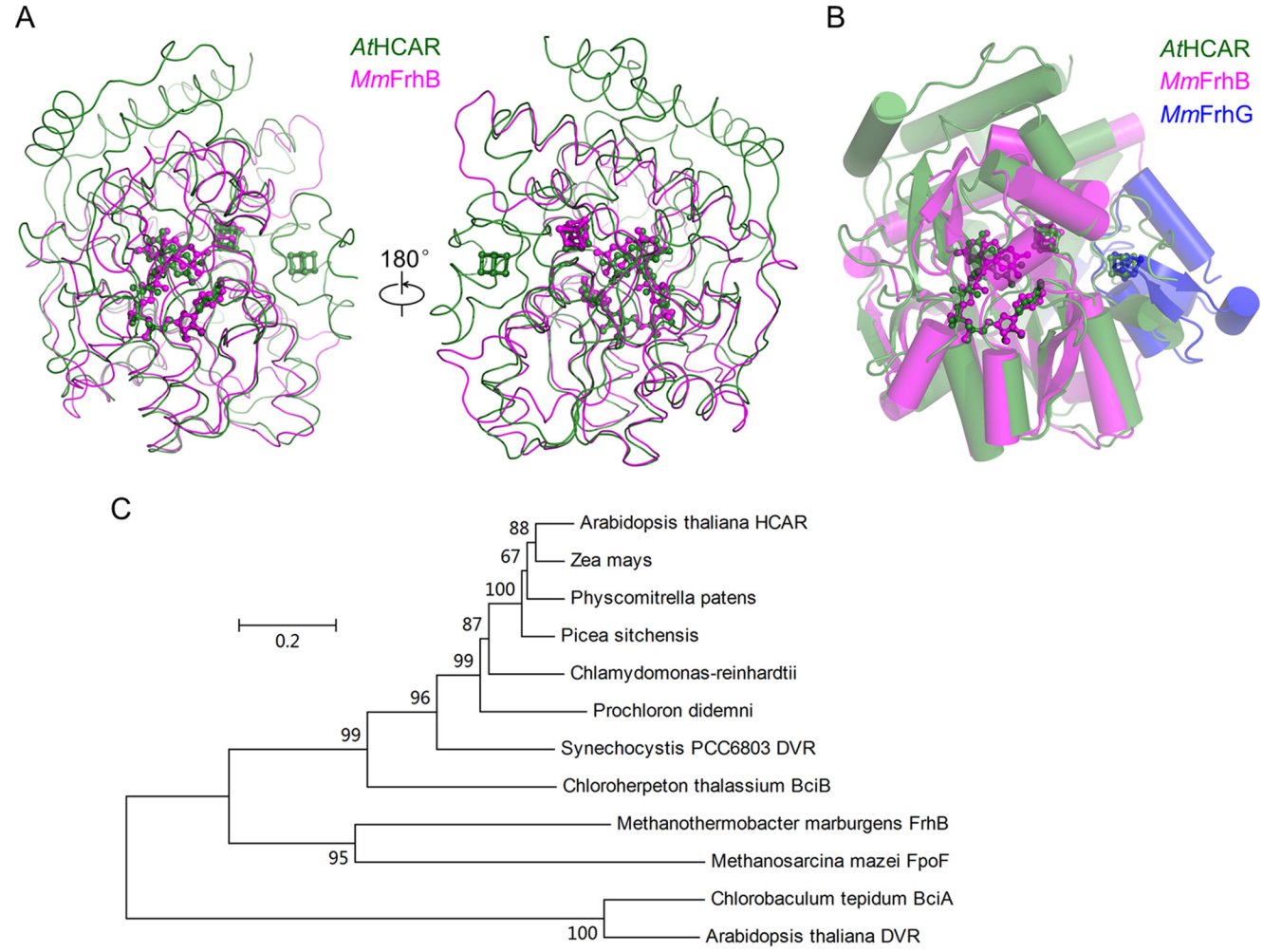

FIGURE 8. **HCAR homologues and evolution.** *A*, superimposition of HCAR with FrhB from *M. marburgensis*. The backbone is shown in tube representation, and the cofactors are in ball-and-stick model. *B*, superimposition of HCAR with FrhB and FrhG from *M. marburgensis*. Each molecule is color-coded. *C*, phylogenetic tree of HCAR homologues. *Chlorobaculum tepidum* BciA and *A. thaliana* DVR are listed as outgroup.

interface between the central and the substrate-binding modules, a second [4Fe-4S] cluster bridges the first [4Fe-4S] cluster with FAD. Both [4Fe-4S] clusters and FAD have clear electron density (Fig. 3*D*). The second [4Fe-4S] cluster is referred to as the proximal cluster for it is closer to FAD. The [4Fe-4S] cluster, typically with a redox potential of approximately −400 mV, mainly functions in electron transfer (40). This crystal structure provides the first definitive evidence of two [4Fe-4S] clusters in HCAR.

Arrangement of Cofactors—All residues involved in cofactor interactions are well defined. The two [4Fe-4S] clusters are coordinated by four cysteines, respectively (Fig. 4*A*). To evaluate the roles of these two clusters, we mutated the ligating cysteines to serines to eliminate each cluster separately. However, the two 4-Cys mutants formed inclusion bodies, and the eight single Cys mutants aggregated. This indicates that both [4Fe-4S] clusters are critical for maintaining protein structure.

The U-shaped FAD is buried inside a cavity of approximate $20 \times 19 \times 8$ Å^3 in the central module (Fig. 4*B*). The U-shaped conformation allows close proximity between the adenine and flavin rings (41). The pyrophosphate moiety is fixed by the backbone amide groups of Gln^{131}–Thr^{137} and Gly^{181} (Fig. 4*C*). The flavin ring is stabilized by amide groups of Tyr^{316} and Met^{317}, and the ribitol moiety forms hydrogen bonds with the side chains of Glu^{262} and Gln^{332}. Hydrogen bonds also occur between 2′-OH of adenosine ribose and the backbone amide group of Val^{155} and between the adenosine ring and the carbonyl groups of Lys^{183} and Thr^{185}. In the crystal, FAD molecules from six HCAR in an asymmetric unit display a uniform binding mode.

Substrate Pocket—The substrate-binding module has a pocket with a size of approximate $18 \times 15 \times 8$ Å^3 (Fig. 5*A*). This hydrophobic pocket with a solvent-accessible entrance is constituted by aromatic residues including Phe^{366} on α9; Phe^{409}, Tyr^{412}, and Tyr^{416} on α11 and Phe^{247}, Tyr^{261}, Phe^{263}, Tyr^{267}, Tyr^{283}, Phe^{284}, and Tyr^{300} in the insertion region, as well as aliphatic residues including Ile^{395} and Leu^{399} on α10 and Val^{236}, Leu^{286}, Leu^{291}, Val^{292}, Val^{294}, and Ile^{295} in the insertion region (Fig. 5*B*). His^{417} is located at the center of the observed substrate pocket, and it may stabilize the Mg^{2+} at the center of the chlorophyll molecule. Using *in silico* docking, we modeled an HMChlide into HCAR. The docked molecule fits well with the substrate pocket, and its 7-hydroxymethyl oxygen atom points to the N_5 atom of the flavin ring, implying an

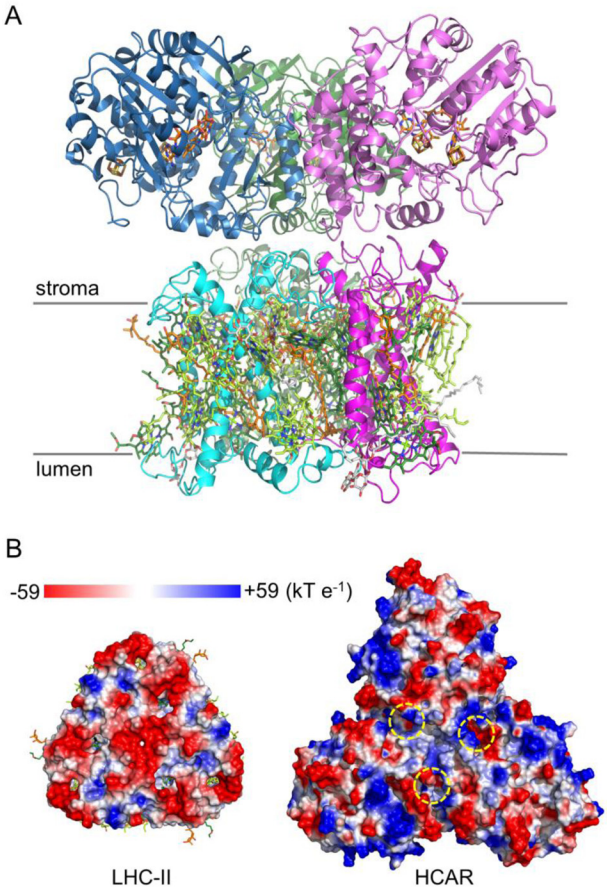

FIGURE 9. **Putative interaction between LHC-II and HCAR.** *A*, model of LHC-II-HCAR complex; view along the thylakoid membrane. LHC-II protomers are colored in *light green*, *cyan*, and *magenta*, respectively. The chlorophyll *a*, chlorophyll *b*, carotenoid, and lipid molecules are shown in *pale green*, *green*, *orange*, and *gray sticks*. HCAR protomers are colored as in Fig. 3*A*. *B*, the putative interacting surface in its electrostatic potentials. The entrances of the substrate pockets of HCAR are indicated by *yellow dashed circles*.

effective electron transfer pathway (Fig. 5*C*). Most of the above mentioned residues are conserved (Fig. 6), indicating a common chlorophyll-binding mode for HCAR homologues from different species.

Catalytic Mechanism—To test the role of the His^{417}, we generated H417A, H417N, and H417Y mutants for activity assays. The H417A mutant formed inclusion bodies during expression, and hence its activity was not measured. Both H417N and H417Y mutants lost their activities (Fig. 7*A*), which highlights the importance of this histidine. Asp^{237}, a residue near His^{417}, is a candidate involved in proton coupling. We generated the D237A mutant, and it lost activity (Fig. 7*A*). The redox cofactor FAD is required to be fine-positioned for efficient electron transfer. Glu^{262} and Gln^{332} are involved in FAD binding through their polar side chains, whereas all other above-mentioned residues stabilize FAD through their backbone atoms (Fig. 4*C*). The E262A mutant lost its catalytic activity, probably for its impaired FAD binding capacity as shown by the spectroscopic analysis (Fig. 7, *A* and *B*). The Q332A mutant aggregated, and its activity was not measured.

The edge to edge distances between the two [4Fe-4S] clusters and between the proximal [4Fe-4S] and FAD are 5.85 ± 0.04 and 3.40 ± 0.05 Å, respectively (Fig. 7*C*). The predicted distance between the substrate carbon-oxygen bond and the N_5 atom of the flavin ring is ~4.4–5.0 Å. Electron transfer could happen directly within such short distances (42). Based on the structure and *in vitro* assay, a detailed proton-activated electron transfer pathway can be suggested (Fig. 7*D*).

HCAR Homologues and Evolution—Homologues of HCAR are distributed from archaea to land plants (15), and their functions have varied widely. The closest structural homologue of HCAR is FrhB from the methanogenic archaeon *M. marburgensis* (20–22). Superimposition of HCAR with FrhB (21) shows the structural similarity of their U-shaped FAD binding site (Fig. 8*A*). Frh catalyzes the reversible redox reaction from H_2 and the cofactor F_{420}, a 5-deazaflavin derivative to $F_{420}H_2$ (43). The root mean square deviation for the 248 aligned Cα atoms between HCAR and FrhB is 2.1 Å. The location of the FrhB [4Fe-4S] cluster is almost identical to the proximal cluster of HCAR (Fig. 8*A*). HCAR has a long N-terminal module holding the distal [4Fe-4S] cluster and a deep substrate pocket. The distal cluster of HCAR overlaps well with the distal [4Fe-4S] cluster in the C-terminal region of FrhG, a subunit that interacts with FrhB in an Frh heterotrimer (Fig. 8*B*). The C-terminal region of FrhG harbors a ferredoxin domain (20–22). Comparably, the N-terminal module of HCAR may interact or correlate with ferredoxin.

The homologue of HCAR in green sulfur bacteria, BciB, is a DVR (19). In the cyanobacterium *Synechocystis*, the HCAR homologue possesses promiscuous enzymatic activities besides its primary function as an DVR and can work as NADH dehydrogenase, chlorophyll *b* reductase, and HCAR (17, 19, 44). Plant HCAR is proposed to evolve from a cyanobacterial DVR with its substrate specificity changing from the 8-vinyl group to the 7-hydroxymethyl group on the chlorin ring, and the neutral NADH dehydrogenase activity is retained (44). A phylogenetic analysis indicates that FrhB and the *bciB*-coded DVR from green sulfur bacteria and most cyanobacteria share a common ancestor with HCAR (Fig. 8*C*). The substrate specificity of HCAR homologues has changed from F_{420} to either the 8-vinyl group or the 7-hydroxymethyl group of (bacterio)chlorophyll, whereas the function as electron input module and the usage of Fd_{red} as electron donor are kept.

Discussion

HCAR is proposed to use proton-coupled electron transfer (PCET) to overcome the carbon-oxygen bond energy barrier in the 7-hydroxymethyl group (10). A similar biological example is ribonucleotide reductase that catalyzes the replacement of the ribose 2′-OH with a hydrogen atom in ribonucleotides by utilizing a PCET pathway via amino acid radicals (45). PCET is a strategy that has been found in metalloenzyme-catalyzed bioenergetics reactions, such as hydrogen oxidation in hydrogenase (43, 46), oxygen reduction in cytochrome *c* oxidase (47), and water oxidation in photosystem II (48). Although the detailed mechanism of PCET is currently under investigation, its fundamental principle is the coupling of electron and proton transfer to cross the intermediate energy barrier (49). The HCAR-catalyzed hydroxymethyl reduction, in which a resonance-stabilized carbocation could exist as intermediate (10, 50), employs proton-activated electron transfer, a type of PCET occurring in

the Q-cycle of the cytochrome bc_1 complex (51). The solvent provides the coupled proton directly or indirectly through neighboring residue(s) (50). We propose that electron donated by Fd_{red} is transferred to FAD via the distal and proximal [4Fe-4S] clusters sequentially and finally to the 7-hydroxymethyl group on the chlorin ring (Fig. 7, *C* and *D*). Physiologically, such a consecutive and direct electron pathway within HCAR ensures a safe path of electron to the target site in an oxygenic environment in plant chloroplasts.

The 3-fold symmetry observed in the HCAR trimer (Fig. 3*A*) is reminiscent of trimerization of LHC-II in plants (52). Because chlorophyll *b* degradation is essential for LHC-II turnover (11–13), and HCAR directly interacts with LHC-II (14), it is plausible that their similarity reflects a biological function (Fig. 9*A*). A comparison of the LHC-II stromal surface (53) and the HCAR surface with substrate pockets reveals an electrostatic complementary between them (Fig. 9*B*). Further studies are needed to elucidate the details of the LHC-II-HCAR interaction. It should be noticed that plant chlorophyll *a* oxygenase is also predicted to be trimeric (54). In summary, our structural and biochemical analysis provides a deeper understanding and a broader scope for the HCAR-catalyzing reaction.

Author Contributions—W. X. performed the experiments; W. X. and L. L. designed the study and wrote the paper.

Acknowledgments—We thank Ming-Zhu Wang at the Institute of Biophysics of the Chinese Academy of Sciences and the staff at Shanghai Synchrotron Radiation Facility for technical support during data collection.

References

1. Mochizuki, N., Tanaka, R., Grimm, B., Masuda, T., Moulin, M., Smith, A. G., Tanaka, A., and Terry, M. J. (2010) The cell biology of tetrapyrroles: a life and death struggle. *Trends Plant Sci.* **15,** 488–498
2. Rüdiger, W. (2002) Biosynthesis of chlorophyll *b* and the chlorophyll cycle. *Photosynth. Res.* **74,** 187–193
3. Hörtensteiner, S. (2006) Chlorophyll degradation during senescence. *Annu. Rev. Plant Biol.* **57,** 55–77
4. Tanaka, R., and Tanaka, A. (2007) Tetrapyrrole biosynthesis in higher plants. *Annu. Rev. Plant Biol.* **58,** 321–346
5. Hörtensteiner, S., and Kräutler, B. (2011) Chlorophyll breakdown in higher plants. *Biochim. Biophys. Acta* **1807,** 977–988
6. Tanaka, R., and Tanaka, A. (2011) Chlorophyll cycle regulates the construction and destruction of the light-harvesting complexes. *Biochim. Biophys. Acta* **1807,** 968–976
7. Tanaka, A., Ito, H., Tanaka, R., Tanaka, N. K., Yoshida, K., and Okada, K. (1998) Chlorophyll *a* oxygenase (CAO) is involved in chlorophyll *b* formation from chlorophyll *a*. *Proc. Natl. Acad. Sci. U.S.A.* **95,** 12719–12723
8. Espineda, C. E., Linford, A. S., Devine, D., and Brusslan, J. A. (1999) The *AtCAO* gene, encoding chlorophyll *a* oxygenase, is required for chlorophyll *b* synthesis in *Arabidopsis thaliana*. *Proc. Natl. Acad. Sci. U.S.A.* **96,** 10507–10511
9. Kusaba, M., Ito, H., Morita, R., Iida, S., Sato, Y., Fujimoto, M., Kawasaki, S., Tanaka, R., Hirochika, H., Nishimura, M., and Tanaka, A. (2007) Rice NON-YELLOW COLORING1 is involved in light-harvesting complex II and grana degradation during leaf senescence. *Plant Cell* **19,** 1362–1375
10. Meguro, M., Ito, H., Takabayashi, A., Tanaka, R., and Tanaka, A. (2011) Identification of the 7-hydroxymethyl chlorophyll *a* reductase of the chlorophyll cycle in *Arabidopsis*. *Plant Cell* **23,** 3442–3453
11. Horie, Y., Ito, H., Kusaba, M., Tanaka, R., and Tanaka, A. (2009) Participation of chlorophyll *b* reductase in the initial step of the degradation of light-harvesting chlorophyll *a*/*b*-protein complexes in *Arabidopsis*. *J. Biol. Chem.* **284,** 17449–17456
12. Shimoda, Y., Ito, H., and Tanaka, A. (2012) Conversion of chlorophyll *b* to chlorophyll *a* precedes magnesium dechelation for protection against necrosis in *Arabidopsis*. *Plant J.* **72,** 501–511
13. Sakuraba, Y., Schelbert, S., Park, S. Y., Han, S. H., Lee, B. D., Andrès, C. B., Kessler, F., Hörtensteiner, S., and Paek, N. C. (2012) STAY-GREEN and chlorophyll catabolic enzymes interact at light-harvesting complex II for chlorophyll detoxification during leaf senescence in *Arabidopsis*. *Plant Cell* **24,** 507–518
14. Sakuraba, Y., Kim, Y. S., Yoo, S. C., Hörtensteiner, S., and Paek, N. C. (2013) 7-Hydroxymethyl chlorophyll *a* reductase functions in metabolic channeling of chlorophyll breakdown intermediates during leaf senescence. *Biochem. Biophys. Res. Commun.* **430,** 32–37
15. Islam, M. R., Aikawa, S., Midorikawa, T., Kashino, Y., Satoh, K., and Koike, H. (2008) slr1923 of *Synechocystis* sp. PCC6803 is essential for conversion of 3,8-divinyl(proto)chlorophyll(ide) to 3-monovinyl(proto)chlorophyll (ide). *Plant Physiol.* **148,** 1068–1081
16. Künkel, A., Vorholt, J. A., Thauer, R. K., and Hedderich, R. (1998) An *Escherichia coli* hydrogenase-3-type hydrogenase in methanogenic archaea. *Eur. J. Biochem.* **252,** 467–476
17. Ito, H., Yokono, M., Tanaka, R., and Tanaka, A. (2008) Identification of a novel vinyl reductase gene essential for the biosynthesis of monovinyl chlorophyll in *Synechocystis* sp. PCC6803. *J. Biol. Chem.* **283,** 9002–9011
18. Liu, Z., and Bryant, D. A. (2011) Multiple types of 8-vinyl reductases for (bacterio)chlorophyll biosynthesis occur in many green sulfur bacteria. *J. Bacteriol.* **193,** 4996–4998
19. Saunders, A. H., Golbeck, J. H., and Bryant, D. A. (2013) Characterization of BciB: a ferredoxin-dependent 8-vinyl-protochlorophyllide reductase from the green sulfur bacterium *Chloroherpeton thalassium*. *Biochemistry* **52,** 8442–8451
20. Mills, D. J., Vitt, S., Strauss, M., Shima, S., and Vonck, J. (2013) *De novo* modeling of the F_{420}-reducing [NiFe]-hydrogenase from a methanogenic archaeon by cryo-electron microscopy. *eLife* **2,** e00218
21. Vitt, S., Ma, K., Warkentin, E., Moll, J., Pierik, A. J., Shima, S., and Ermler, U. (2014) The F_{420}-reducing [NiFe]-hydrogenase complex from *Methanothermobacter marburgensis*, the first x-ray structure of a group 3 family member. *J. Mol. Biol.* **426,** 2813–2826
22. Allegretti, M., Mills, D. J., McMullan, G., Kühlbrandt, W., and Vonck, J. (2014) Atomic model of the F_{420}-reducing [NiFe] hydrogenase by electron cryo-microscopy using a direct electron detector. *eLife* **3,** e01963
23. Pryor, K. D., and Leiting, B. (1997) High-level expression of soluble protein in *Escherichia coli* using a His_6-tag and maltose-binding-protein double-affinity fusion system. *Protein Expr. Purif.* **10,** 309–319
24. Terwilliger, T. C., Adams, P. D., Read, R. J., McCoy, A. J., Moriarty, N. W., Grosse-Kunstleve, R. W., Afonine, P. V., Zwart, P. H., and Hung, L. W. (2009) Decision-making in structure solution using Bayesian estimates of map quality: the PHENIX AutoSol wizard. *Acta Crystallogr. D Biol. Crystallogr.* **65,** 582–601
25. Adams, P. D., Afonine, P. V., Bunkóczi, G., Chen, V. B., Davis, I. W., Echols, N., Headd, J. J., Hung, L. W., Kapral, G. J., Grosse-Kunstleve, R. W., McCoy, A. J., Moriarty, N. W., Oeffner, R., Read, R. J., Richardson, D. C., *et al.* (2010) PHENIX: a comprehensive Python-based system for macromolecular structure solution. *Acta Crystallogr. D Biol. Crystallogr.* **66,** 213–221
26. Terwilliger, T. C., Grosse-Kunstleve, R. W., Afonine, P. V., Moriarty, N. W., Zwart, P. H., Hung, L. W., Read, R. J., and Adams, P. D. (2008) Iterative model building, structure refinement and density modification with the PHENIX AutoBuild wizard. *Acta Crystallogr. D Biol. Crystallogr.* **64,** 61–69
27. Emsley, P., Lohkamp, B., Scott, W. G., and Cowtan, K. (2010) Features and development of Coot. *Acta Crystallogr. D Biol. Crystallogr.* **66,** 486–501
28. Afonine, P. V., Grosse-Kunstleve, R. W., Echols, N., Headd, J. J., Moriarty, N. W., Mustyakimov, M., Terwilliger, T. C., Urzhumtsev, A., Zwart, P. H., and Adams, P. D. (2012) Towards automated crystallographic structure refinement with phenix.refine. *Acta Crystallogr. D Biol. Crystallogr.* **68,** 352–367
29. Chen, V. B., Arendall, W. B., 3rd, Headd, J. J., Keedy, D. A., Immormino, R. M., Kapral, G. J., Murray, L. W., Richardson, J. S., and Richardson, D. C.

(2010) MolProbity: all-atom structure validation for macromolecular crystallography. *Acta Crystallogr. D Biol. Crystallogr.* **66,** 12–21
30. Trott, O., and Olson, A. J. (2010) AutoDock Vina: improving the speed and accuracy of docking with a new scoring function, efficient optimization, and multithreading. *J. Comput. Chem.* **31,** 455–461
31. Morris, G. M., Huey, R., Lindstrom, W., Sanner, M. F., Belew, R. K., Goodsell, D. S., and Olson A. J. (2009) AutoDock4 and AutoDockTools4: Automated docking with selective receptor flexibility. *J. Comput. Chem.* **30,** 2785–2791
32. Holt, A. S. (1959) Reduction of chlorophyllides, chlorophylls and chlorophyll derivatives by sodium borohydride. *Plant Physiol.* **34,** 310–314
33. Porra, R. J., Thompson, W. A., and Kriedemann, P. E. (1989) Determination of accurate extinction coefficients and simultaneous equations for assaying chlorophylls *a* and *b* extracted with four different solvents: verification of the concentration of chlorophyll standards by atomic absorption spectroscopy. *Biochim. Biophys. Acta* **975,** 384–394
34. Ito, H., Ohtsuka, T., and Tanaka, A. (1996) Conversion of chlorophyll *b* to chlorophyll *a* via 7-hydroxymethyl chlorophyll. *J. Biol. Chem.* **271,** 1475–1479
35. Sievers, F., Wilm, A., Dineen, D., Gibson, T. J., Karplus, K., Li, W., Lopez, R., McWilliam, H., Remmert, M., Söding, J., Thompson, J. D., and Higgins, D. G. (2011) Fast, scalable generation of high-quality protein multiple sequence alignments using Clustal Omega. *Mol. Syst. Biol.* **7,** 539
36. Touw, W. G., Baakman, C., Black, J., te Beek, T. A., Krieger, E., Joosten, R. P., and Vriend, G. (2015) A series of PDB-related databanks for everyday needs. *Nucleic Acids Res.* **43,** D364–D368
37. Robert, X., and Gouet, P. (2014) Deciphering key features in protein structures with the new ENDscript server. *Nucleic Acids Res.* **42,** W320–W324
38. Tamura, K., Dudley, J., Nei, M., and Kumar, S. (2007) MEGA4: Molecular Evolutionary Genetics Analysis (MEGA) software version 4.0. *Mol. Biol. Evol.* **24,** 1596–1599
39. Hendrickson, W. A. (1991) Determination of macromolecular structures from anomalous diffraction of synchrotron radiation. *Science* **254,** 51–58
40. Beinert, H. (2000) Iron-sulfur proteins: ancient structures, still full of surprises. *J. Biol. Inorg. Chem.* **5,** 2–15
41. Dym, O., and Eisenberg, D. (2001) Sequence-structure analysis of FAD-containing proteins. *Protein Sci.* **10,** 1712–1728
42. Page, C. C., Moser, C. C., Chen, X., and Dutton, P. L. (1999) Natural engineering principles of electron tunnelling in biological oxidation-reduction. *Nature* **402,** 47–52
43. Thauer, R. K., Kaster, A. K., Goenrich, M., Schick, M., Hiromoto, T., and Shima, S. (2010) Hydrogenases from methanogenic archaea, nickel, a novel cofactor, and H_2 storage. *Annu. Rev. Biochem.* **79,** 507–536
44. Ito, H., and Tanaka, A. (2014) Evolution of a new chlorophyll metabolic pathway driven by the dynamic changes in enzyme promiscuous activity. *Plant Cell Physiol.* **55,** 593–603
45. Cotruvo, J. A., and Stubbe, J. (2011) Class I ribonucleotide reductases: metallocofactor assembly and repair *in vitro* and *in vivo*. *Annu. Rev. Biochem.* **80,** 733–767
46. Peters, J. W., Schut, G. J., Boyd, E. S., Mulder, D. W., Shepard, E. M., Broderick, J. B., King, P. W., and Adams, M. W. (2015) [FeFe]- and [NiFe]-hydrogenase diversity, mechanism, and maturation. *Biochim. Biophys. Acta* **1853,** 1350–1369
47. Belevich, I., Verkhovsky, M. I., and Wikström, M. (2006) Proton-coupled electron transfer drives the proton pump of cytochrome *c* oxidase. *Nature* **440,** 829–832
48. Umena, Y., Kawakami, K., Shen, J. R., and Kamiya, N. (2011) Crystal structure of oxygen-evolving photosystem II at a resolution of 1.9 Å. *Nature* **473,** 55–60
49. Weinberg, D. R., Gagliardi, C. J., Hull, J. F., Murphy, C. F., Kent, C. A., Westlake, B. C., Paul, A., Ess, D. H., McCafferty, D. G., and Meyer, T. J. (2012) Proton-coupled electron transfer. *Chem. Rev.* **112,** 4016–4093
50. Folly, P., and Engel, N. (1999) Chlorophyll *b* to chlorophyll *a* conversion precedes chlorophyll degradation in *Hordeum vulgare* L. *J. Biol. Chem.* **274,** 21811–21816
51. Migliore, A., Polizzi, N. F., Therien, M. J., and Beratan, D. N. (2014) Biochemistry and theory of proton-coupled electron transfer. *Chem. Rev.* **114,** 3381–3465
52. Dekker, J. P., and Boekema, E. J. (2005) Supramolecular organization of thylakoid membrane proteins in green plants. *Biochim. Biophys. Acta* **1706,** 12–39
53. Liu, Z., Yan, H., Wang, K., Kuang, T., Zhang, J., Gui, L., An, X., and Chang, W. (2004) Crystal structure of spinach major light-harvesting complex at 2.72 Å resolution. *Nature* **428,** 287–292
54. Kunugi, M., Takabayashi, A., and Tanaka A. (2013) Evolutionary changes in chlorophyllide *a* oxygenase (CAO) structure contribute to the acquisition of a new light-harvesting complex in micromonas. *J. Biol. Chem.* **288,** 19330–19341